Supporting Information

Tri-Coordinated Au Dopant Induced Out-of-plane Ferroelectricity and Enhanced Ferromagnetism in Chromium Triiodide

*Lei Zhang [ab], Cheng Tang [ab], Aijun Du [*ab]*

[a] School of Chemistry and Physics, Queensland University of Technology, Gardens Point Campus, Brisbane, QLD 4000, Australia

[b] Centre for Materials Science, Queensland University of Technology, Gardens Point Campus, Brisbane, QLD 4000, Australia
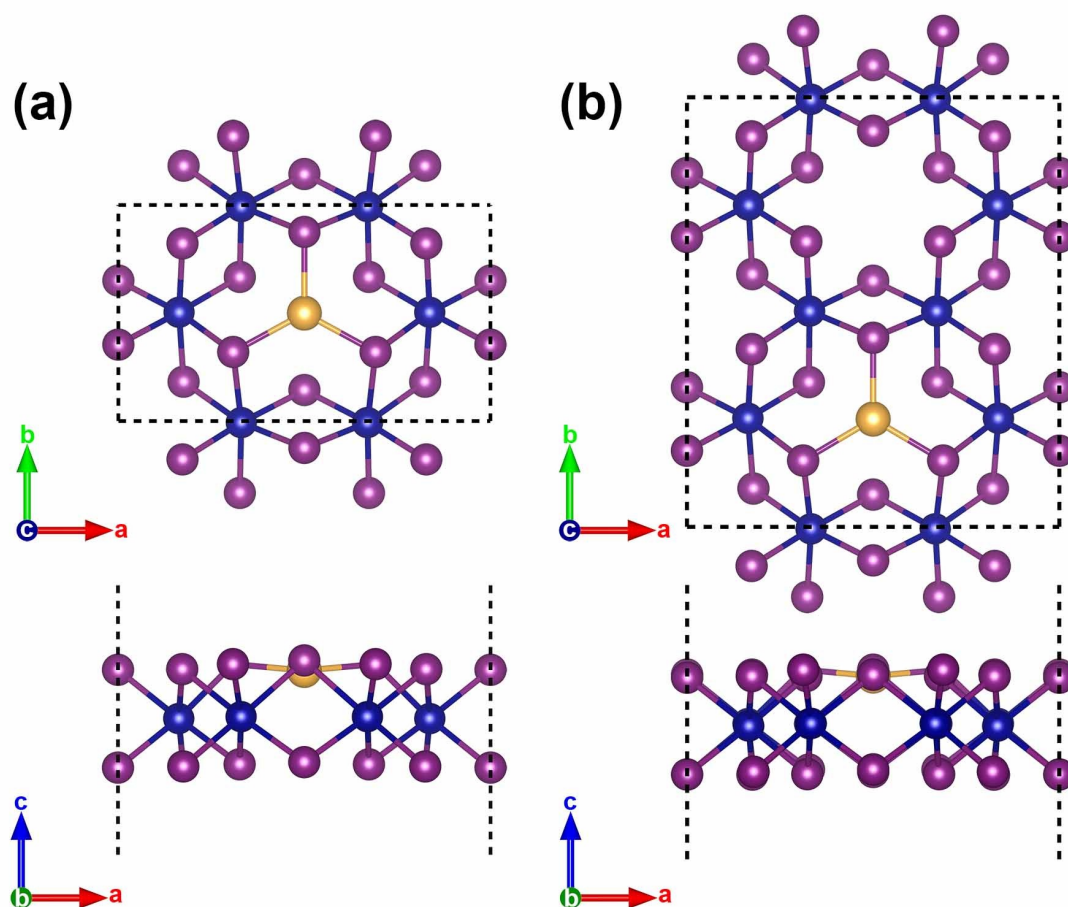
Figure S1. (a) and (b) Atomic structure of 2D FE $Au_{1/4}CrI_3$ and $Au_{1/8}CrI_3$ respectively.

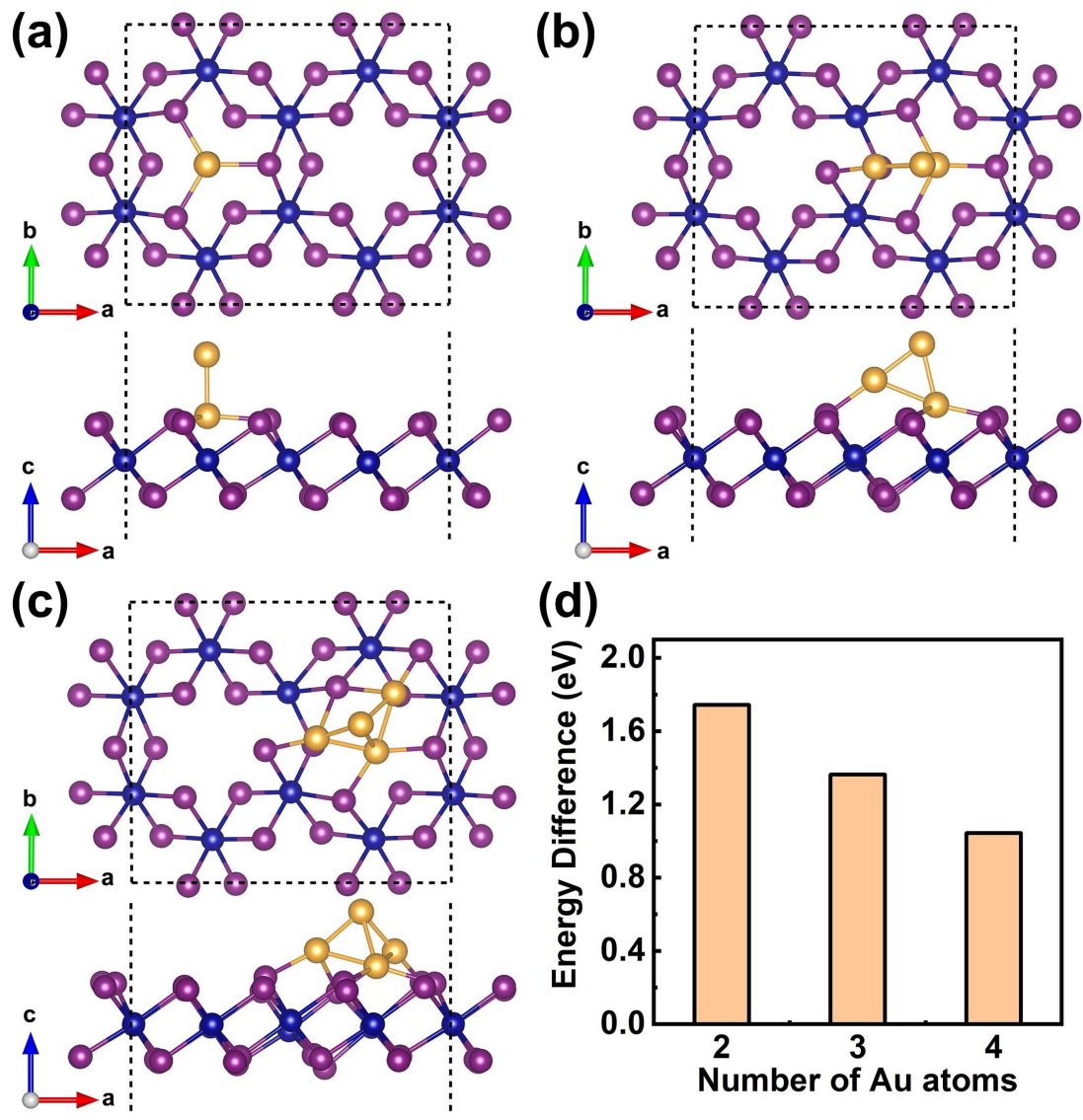**Figure S2.** (a), (b) and (c) The atomic structures of Au_2, Au_3, and Au_4 clusters on 2D CrI_3, respectively. (d) The energy difference between $Au_xCr_8I_{24}$ (x=2, 3, and 4) with Au forming clusters and Au uniformly dispersed in different I_6 hollow sites.
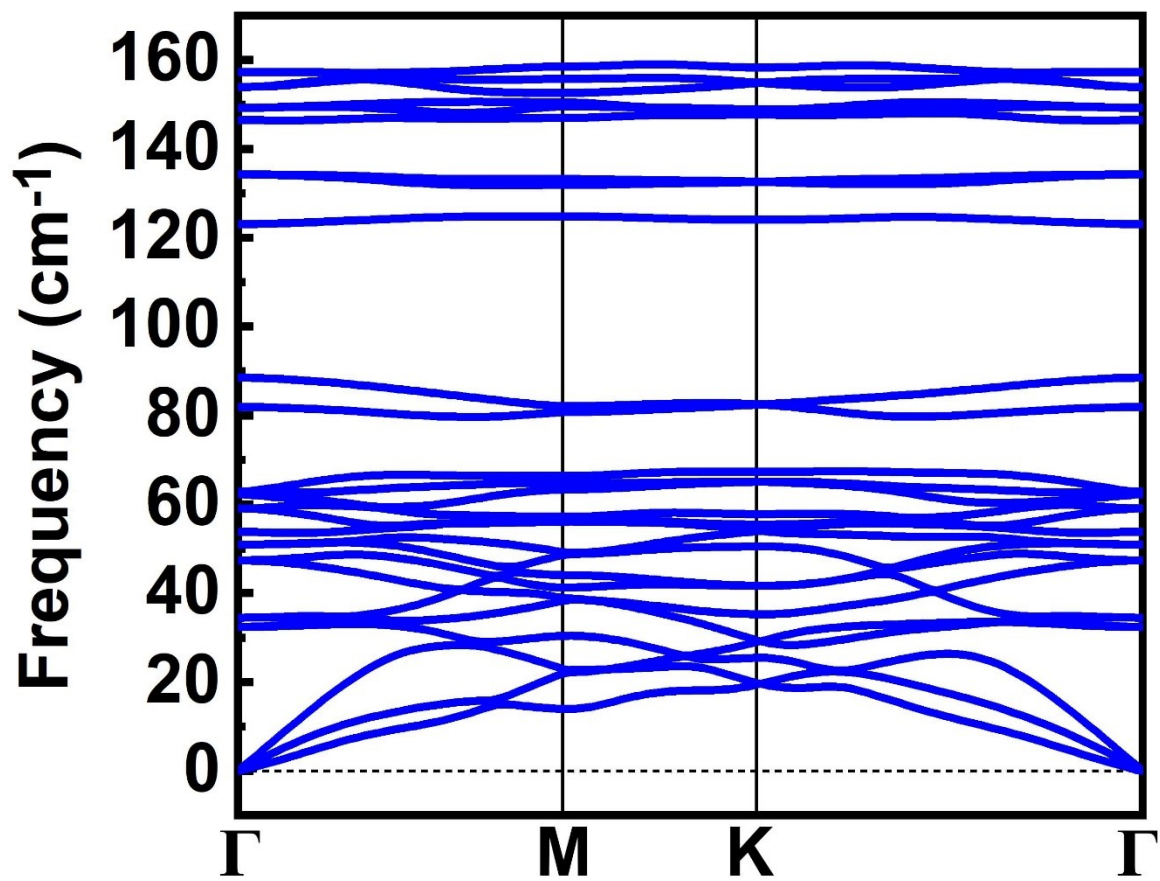
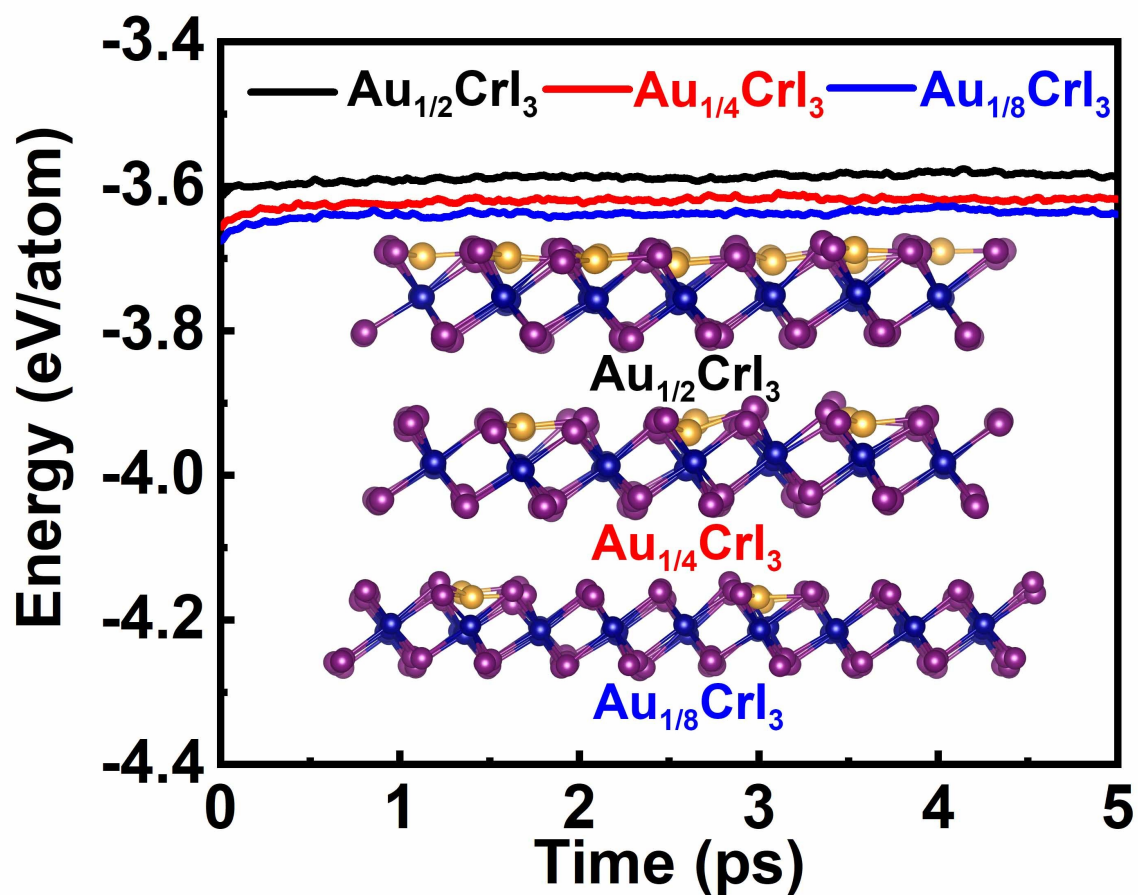**Figure S3.** The phonon spectrum of 2D FE $Au_{1/2}CrI_3$.

Figure S4. The energy of 2D $Au_{1/2}CrI_3$ during the AIMD simulations performed at 300 K for 5 ps. The insets are the final atomic structures at the end of simulations. It can be seen the energy fluctuates within a small range and no Au migration is observed during the AIMD simulations, suggesting the thermal stability of these FE phases.

Note 1

Here we consider the AFE configuration with opposite dipole moments along the direction a, as shown in Figure S5b. We find the AFE configuration is lower in energy by 0.27 eV compared with the FE phase, which is similar to the cases of FE Sc_2CO_2 where the AFE phase is lower in energy by 0.12 eV and FE $CuMP_2X_6$ (M=Cr, V; X=S, Se) where the AFE phases are lower in energy by ~0.14-0.175 eV.[1, 2] The AFE phase possesses a P21/m space group with inversion symmetry, so the overall electric polarization is zero, which may limit its experimental detection. Hence, it is of interest to check whether the AFE phase can be transferred into the FE phase. To clarify this, the energy difference between FE and AFE phases under external electric field E (along the polarization direction in FE phase) and the AFE to FE transition barrier are calculated, as shown in Figures S5c and d, respectively. It can be seen that the energy difference decreases with the increasing E and becomes negligible when E reaches 1 V/Å. The AFE to FE transition barrier is moderate which is determined to be 0.33 eV. These results demonstrate the AFE phases can be transferred into the FE phases using an external electric field. The FE to AFE transition displays an energy barrier of 0.11 eV, thus after the FE phase is obtained, it will not spontaneously transfer into AFE phase. This is also validated by our AIMD simulations for FE phase (Figure S4 in Supporting Information), where no FE to AFE transition is observed.
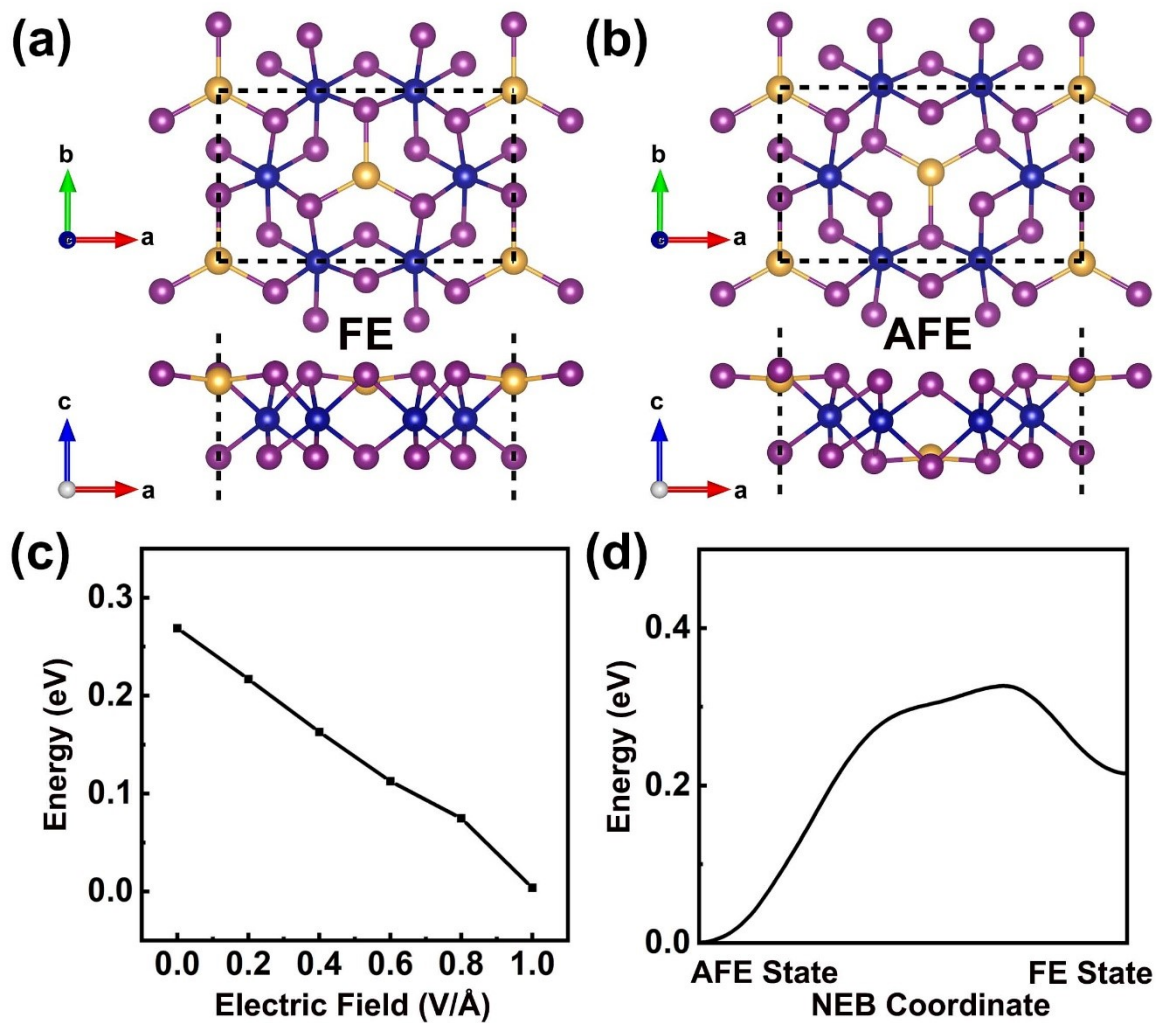
Figure S5. (a) and (b) The atomic structures of FE and AFE phases of $Au_{1/2}CrI_3$. (c) The energy difference between FE and AFE phases of $Au_{1/2}CrI_3$ under electric fields from 0 to 1 V/Å. (d) The energy profile for the AFE to FE phase transition of $Au_{1/2}CrI_3$.
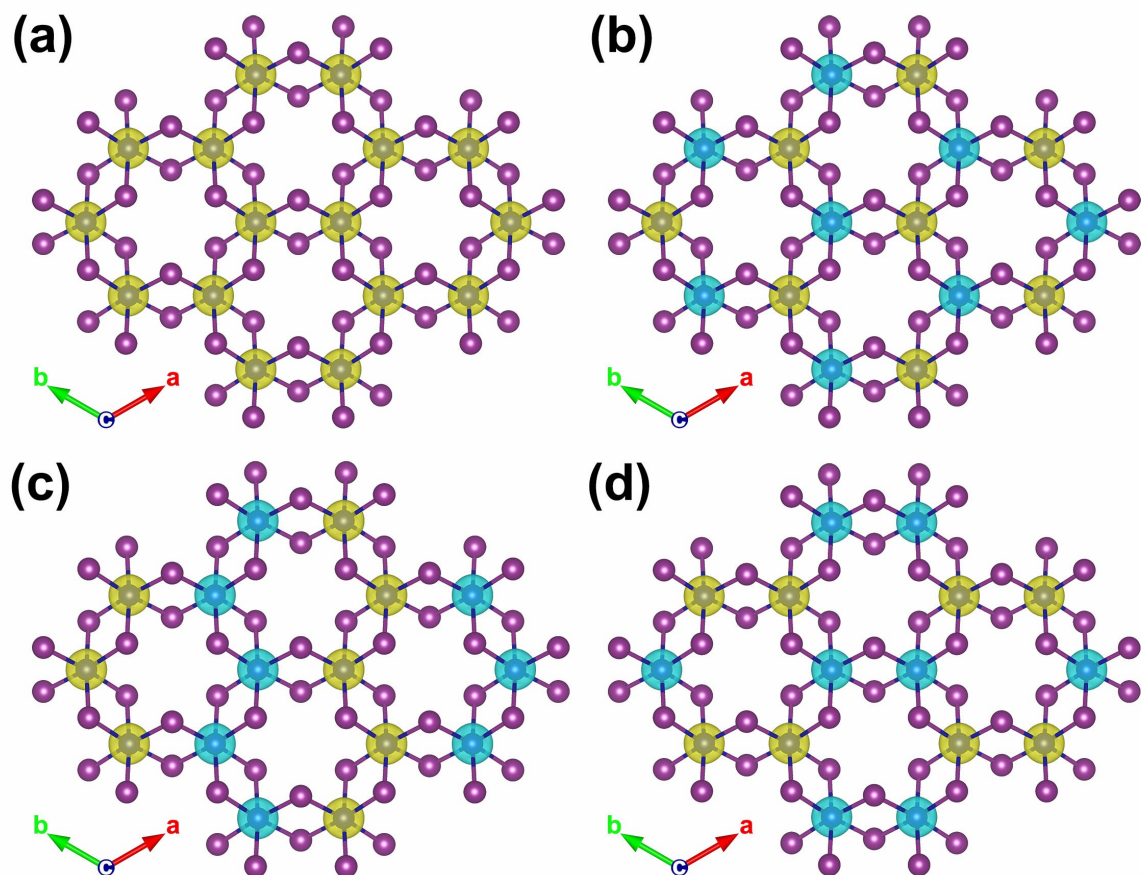
Figure S6. (a)-(d) The spin density of for CrI$_3$ monolayer in FM, Neel AFM, zig-zag AFM, and stripy AFM configurations, respectively. The isosurface value is set to 0.03 electrons per A^3.
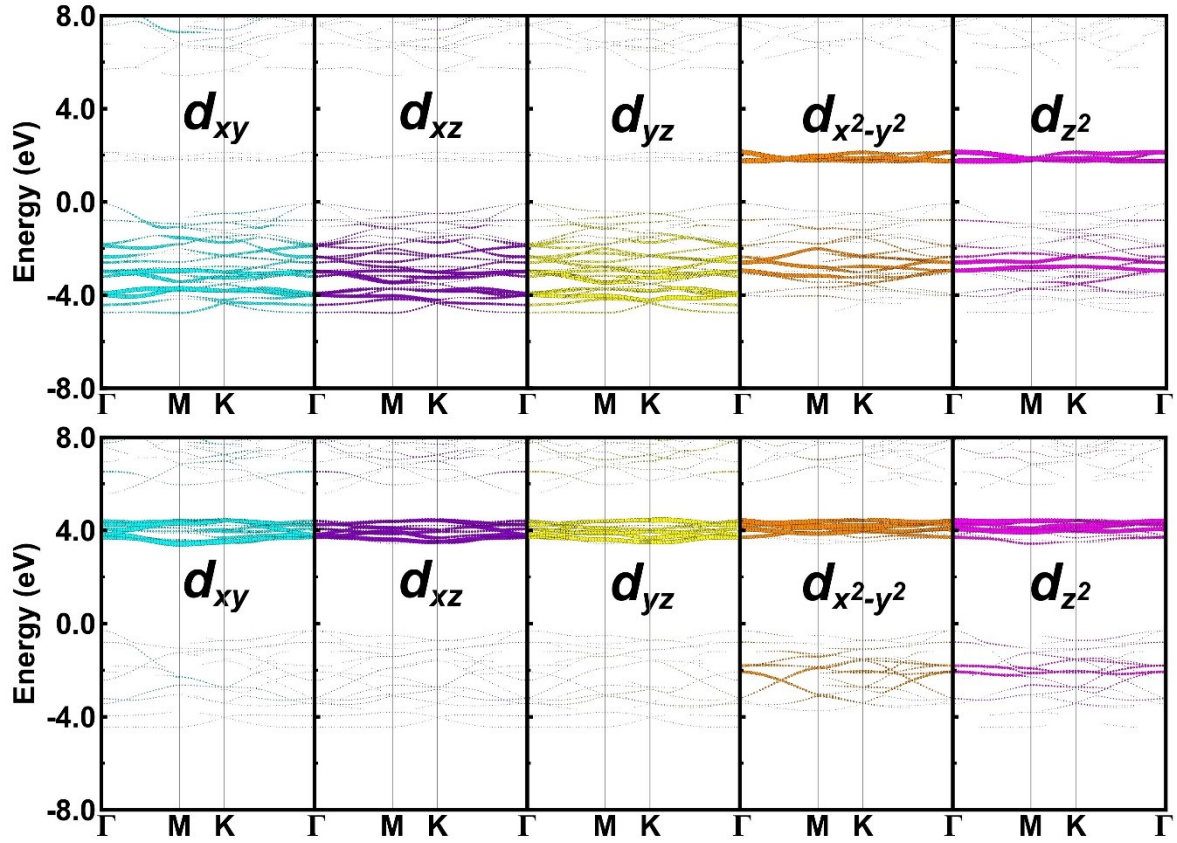
Figure S7. The orbital resolved band structures for Cr-3d orbitals. The upper and lower panels represent the spin-up and spin-down bands respectively.
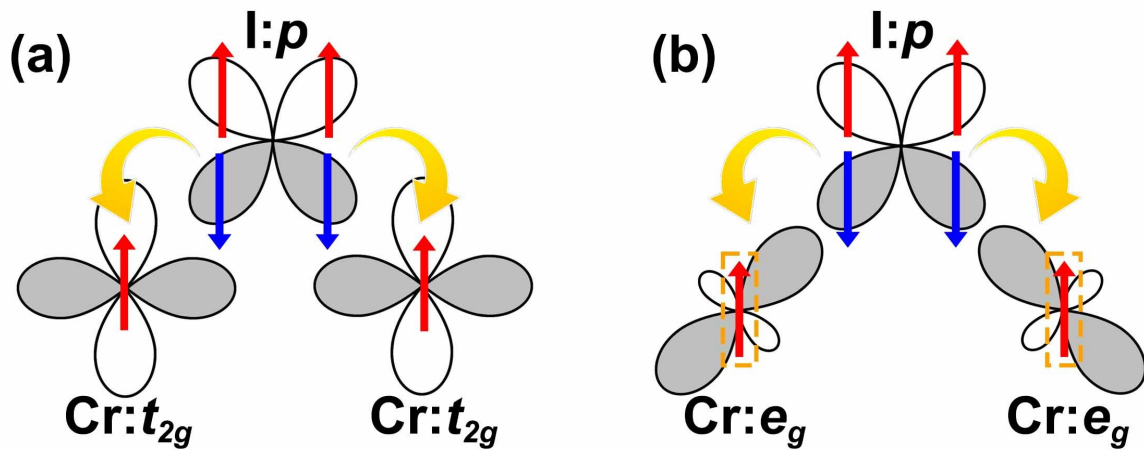

Figure S8. (a) and (b) The schematic representations of the t_{2g}-p-t_{2g} and e_g-p-e_g super-exchange interactions, respectively. The red, blue, and yellow arrows represent the spin-up electrons,

spin-down electrons, and the electron hopping between p and d orbitals. The orange rectangles indicate the partially occupied e_g orbitals.
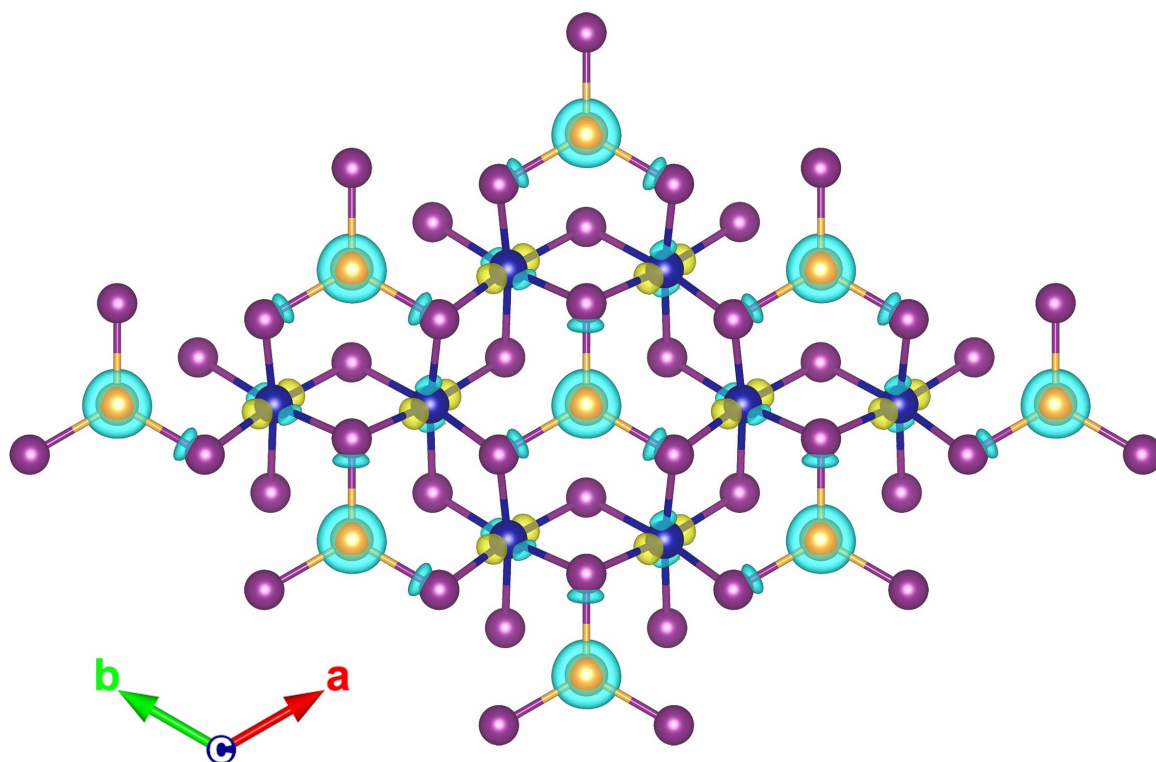

Figure S9. The charge density difference (ρ_{diff}) of $Au_{1/2}CrI_3$ with an isosurface value of 0.006 electrons per A^3. The ρ_{diff} is calculated by $\rho_{diff} = \rho_{Au_{1/2}CrI_3} - \rho_{Au} - \rho_{CrI_3}$ where the $\rho_{Au_{1/2}CrI_3}$, ρ_{Au}, and ρ_{CrI_3} represent the charge density of $Au_{1/2}CrI_3$, Au atom and CrI_3 monolayer, respectively. The yellow and cyan color represents the accumulation and depletion of charge density. It can be seen that the electron density accumulates around the Cr atoms while depletes around the Au atoms, suggesting the Au atoms will donate electrons to the CrI_3 monolayer.
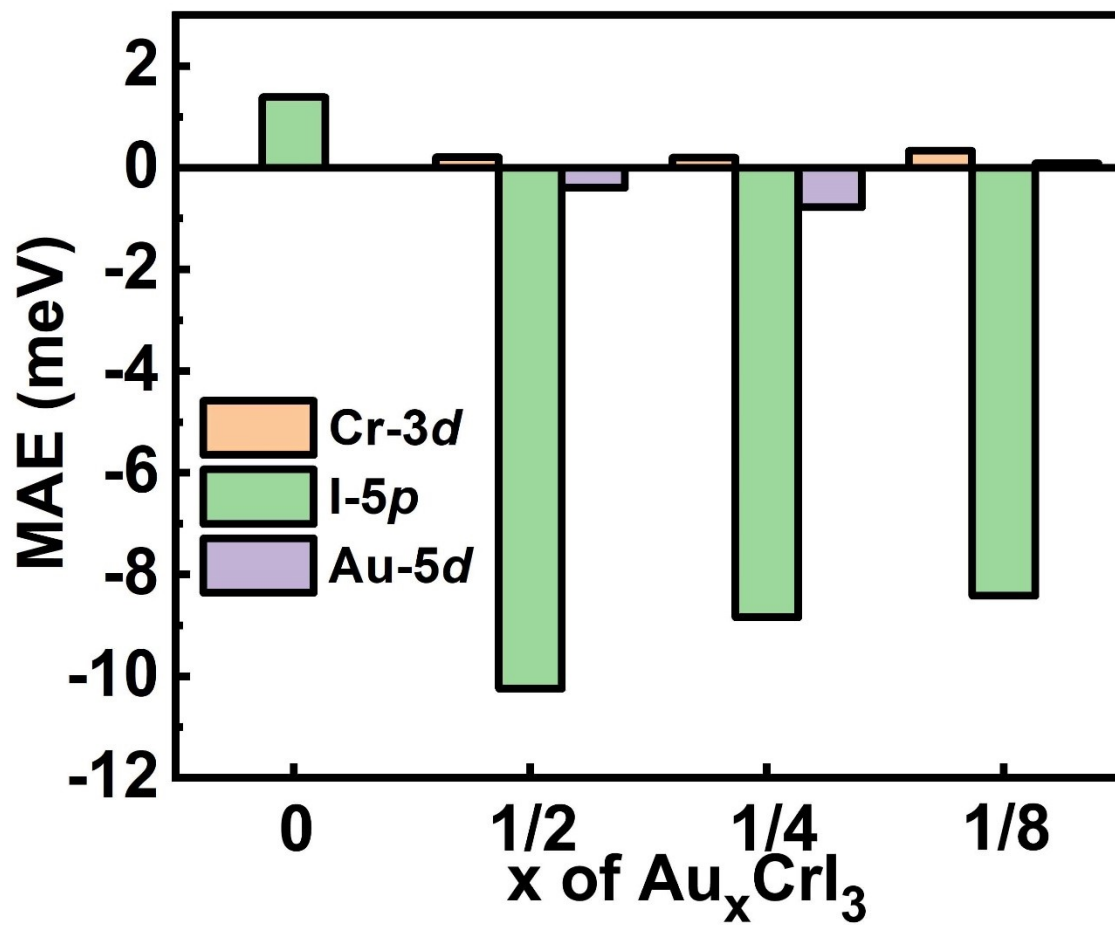
Figure S10. The orbital resolved MAE for CrI_3 and Au doped CrI_3.

Note 2

The transition metal dichalcogenides (TMD) display opposite orbital magnetic moments at +K and –K points, giving rise to inequivalent valleys. The energies of particles in the two valleys are intrinsically degenerate due to the time-reversal symmetry in monolayer TMDs. The degeneracy can be broken by applying magnetic field, which can result in valley polarization. The magnetism of $Au_{1/2}CrI_3$ can be used to break the time-reversal symmetry of TMDs and the switchable electric polarization can be utilized to tune the interlayer coupling, which may enable tunable valley polarization controlled by FE switching. The $2 \times 2 \times 1$ WTe$_2$ show similar lattice constants (7.03 Å) as $1 \times 1 \times 1$ $Au_{1/2}CrI_3$ (7.17 Å), thus we construct WTe$_2$/Au$_{1/2}$CrI$_3\uparrow$ and WTe$_2$/Au$_{1/2}$CrI$_3\downarrow$ heterostructures (the arrows represent the +P and –P states, respectively) to explore the possibility of such magnetoelectric coupling. We adopted the stacking sequence as described in ref. 3 and 4, where the W atoms in located above the center of I_6 hollow site in 2D CrI$_3$, as shown in Figures S11a and c. The Figures S11b and d show the projected band structures of WTe$_2$ on +P and –P $Au_{1/2}CrI_3$ substrate, respectively. Clearly, the valence band maximum (VBM) at +K and –K points show opposite valley pseudospin. A large valley polarization (defined as the energy level difference between the VBM at +K and –K) of 66.36 meV is observed for the +P states, while that for the –P states is only 1.68 meV. Hence, through FE switching, the valley polarization of WTe$_2$ can be efficiently tuned, which may show promising applications in spintronic devices.
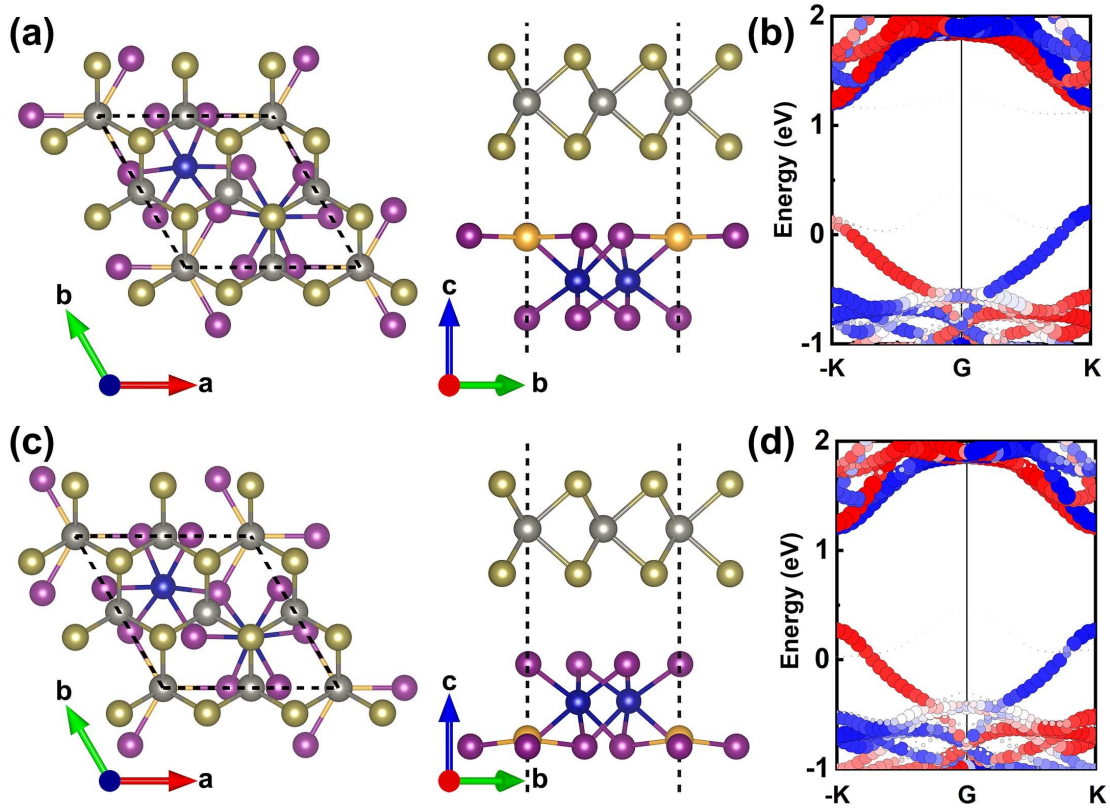
Figure S11. (a) and (c) The atomic positions of $WTe_2/Au_{1/2}CrI_3\uparrow$ and $WTe_2/Au_{1/2}CrI_3\downarrow$ heterostructures, respectively. (b) and (d) The projected band structures of WTe_2 in the $WTe_2/Au_{1/2}CrI_3\uparrow$ and $WTe_2/Au_{1/2}CrI_3\downarrow$ heterostructures, respectively. The S_x component is plotted as the magnetic easy axis lies in the x-direction. The red and blue colors represent the spin-up and spin-down expectation values of spin operator S_x.

References

1. A. Chandrasekaran, A. Mishra and A. K. Singh, Ferroelectricity, Antiferroelectricity, and Ultrathin 2D Electron/Hole Gas in Multifunctional Monolayer MXene. *Nano Letters*, 2017, **17**, 3290-3296.
2. J. Qi, H. Wang, X. Chen and X. Qian, Two-Dimensional Multiferroic Semiconductors with Coexisting Ferroelectricity and Ferromagnetism. *Applied Physics Letters*, 2018, **113**, 043102.
3. M. Ge, H. Wang, J. Wu, C. Si, J. Zhang and S. Zhang, Enhanced Valley Splitting of WSe_2 in Twisted van der Waals WSe_2/CrI_3 Heterostructures. *npj Computational Materials*, 2022, **8**, 32.
4. R. Hidalgo-Sacoto, R. I. Gonzalez, E. E. Vogel, S. Allende, J. D. Mella, C. Cardenas, R. E. Troncoso and F. Munoz, Magnon Valley Hall Effect in CrI_3-Based van der Waals Heterostructures. *Physical Review B*, 2020, **101**, 205425.